A&A 641, A153 (2020)
https://doi.org/10.1051/0004-6361/202038490

Astronomy & Astrophysics

First detection of NHD and ND_2 in the interstellar medium

Amidogen deuteration in IRAS 16293–2422

M. Melosso[1], L. Bizzocchi[2], O. Sipilä[2], B. M. Giuliano[2], L. Dore[1], F. Tamassia[3], M.-A. Martin-Drumel[4], O. Pirali[4,5], E. Redaelli[2], and P. Caselli[2]

[1] Dipartimento di Chimica "Giacomo Ciamician", Università di Bologna, Via F. Selmi 2, 40126 Bologna, Italy
e-mail: mattia.melosso2@unibo.it
[2] Center for Astrochemical Studies, Max-Planck-Institut für extraterrestrische Physik, Gießenbachstraße 1, 85748 Garching, Germany
e-mail: bizzocchi@mpe.mpg.de
[3] Dipartimento di Chimica Industriale "Toso Montanari", Università di Bologna, viale del Risorgimento 4, 40136 Bologna, Italy
[4] Université Paris-Saclay, CNRS, Institut des Sciences Moléculaires d'Orsay, 91405 Orsay Cedex, France
[5] SOLEIL Synchrotron, AILES beamline, l'Orme des Merisiers, Saint-Aubin, 91190 Gif-sur-Yvette, France

Received 26 May 2020 / Accepted 14 July 2020

ABSTRACT

Context. Deuterium fractionation processes in the interstellar medium (ISM) have been shown to be highly efficient in the family of nitrogen hydrides. To date, observations have been limited to ammonia (NH_2D, NHD_2, ND_3) and imidogen radical (ND) isotopologues.
Aims. We want to explore the high-frequency windows offered by the *Herschel* Space Observatory to search for deuterated forms of the amidogen radical NH2 and to compare the observations against the predictions of our comprehensive gas-grain chemical model.
Methods. Making use of the new molecular spectroscopy data recently obtained at high frequencies for NHD and ND_2, we searched for both isotopologues in the spectral survey toward the Class 0 protostar IRAS 16293-2422, a source in which NH_3, NH, and their deuterated variants have previously been detected. We used the observations carried out with HIFI (Heterodyne Instrument for the Far-Infrared) in the framework of the key program "Chemical *Herschel* surveys of star forming regions" (CHESS).
Results. We report the first detection of interstellar NHD and ND_2. Both species are observed in absorption against the continuum of the protostar. From the analysis of their hyperfine structure, accurate excitation temperature and column density values are determined. The latter were combined with the column density of the parent species NH_2 to derive the deuterium fractionation in amidogen. We find a high deuteration level of amidogen radical in IRAS 16293-2422, with a deuterium enhancement about one order of magnitude higher than that predicted by earlier astrochemical models. Such a high enhancement can only be reproduced by a gas-grain chemical model if the pre-stellar phase preceding the formation of the protostellar system has a long duration: on the order of one million years.
Conclusions. The amidogen D/H ratio measured in the low-mass protostar IRAS 16293-2422 is comparable to that derived for the related species imidogen and much higher than that observed for ammonia. Additional observations of these species will provide more insights into the mechanism of ammonia formation and deuteration in the ISM. Finally, we indicate the current possibilities to further explore these species at submillimeter wavelengths.

Key words. astrochemistry – ISM: molecules – line: identification – ISM: abundances – submillimeter: ISM

1. Introduction

Despite the low cosmic abundance of deuterium (D/H = 1.5×10^{-5}, Linsky 2003), deuterated molecules can be found in the interstellar medium (ISM) in enormously large amounts and are routinely used as proxies for the cold environments typical of the early stages of the star formation process. It is well known that deuterium fractionation processes (i.e., the deuterium enrichment in a given molecular species) can occur at a very high rate under certain physical conditions, including, most notably, a low gas temperature (5–20 K) and strong CO depletion (Caselli & Ceccarelli 2012). Inheriting such conditions from their pre-stellar core phase, Class 0 protostars are the astronomical objects that exhibit the largest molecular deuteration found to date (Ceccarelli et al. 2014). In the last few decades, several deuterium-bearing species (including doubly and triply deuterated forms) have been detected in these sources, including water D_2O (Butner et al. 2007), formaldehyde D_2CO (Ceccarelli et al. 1998), hydrogen sulfide D_2S (Vastel et al. 2003), methanol CD_3OH (Parise et al. 2004), and ammonia ND_3 (Roueff et al. 2005; van der Tak et al. 2002).

The Class 0 protostar IRAS 16293-2422, located in the nearby ρ-Ophiuchi star-forming region (at a distance of ~120 pc), is considered a specimen for super-deuteration phenomena (Ceccarelli et al. 2007). Indeed, in addition to having an exceptionally rich chemistry in its inner and warmer regions (van Dishoeck et al. 1995; Jørgensen et al. 2012; Fayolle et al. 2017), this source harbors a large number of interstellar deuterated species in its outer cold envelope (Loinard et al. 2001). Among them, the family of neutral nitrogen hydrides (NH, NH_2, and NH_3) is well-represented, given that all the deuterated forms of ammonia (NH_2D, NHD_2, and ND_3) and the imidogen radical ND (Bacmann et al. 2010, 2016) have been detected so far. However, deuterium enrichment has never been observed for the amidogen radical NH_2, neither in IRAS 16293-2422 nor in any other astronomical sources.

The current lack of observation of interstellar NHD and ND_2 may be attributed to several factors. Until recently, laboratory data were limited to the frequency region below 500 GHz (Kanada et al. 1991; Kobayashi et al. 1997). At low temperatures, neither species possesses any bright transitions in this portion of the spectrum, with *b*-type fundamental transitions lying high into the submillimeter-wave domain (around 770 GHz for NHD and around 527 GHz for ND_2). Furthermore, the amidogen radical is a textbook floppy molecule, for which frequency extrapolation from low-frequency measurements is extremely unreliable. Besides the deficiency of laboratory spectral data, ground-based astronomical observations of these light species are hindered by the atmospheric opacity at submillimeter-wavelengths. Therefore, even with high-frequency facilities (such as ALMA or SOFIA), the observation of light hydrides remains a challenging task. Onboard observations using the *Herschel* Space Observatory mission, during which numerous projects attempted to gain more insights into the chemistry of the ISM, offer a unique chance to overcome the latter issue. Also, now that recent laboratory studies of nitrogen hydrides in their various deuterated forms have been reported up to the terahertz domain (Melosso et al. 2017, 2019a,b, 2020; Bizzocchi et al. 2020), confident searches for these species can be undertaken in *Herschel* archival surveys.

In this paper, we report the first detection of NHD and ND_2 in the ISM, thanks to HIFI[1] observations carried out as part of the CHESS[2] key program (PI: C. Ceccarelli). Both species were observed in absorption against the continuum of the low-luminosity protostar IRAS 16293-2422. From the modeling of NHD and ND_2 hyperfine structures, column densities of the two radicals were determined and the deuterium fractionation of amidogen radical evaluated.

2. Observations

The observations analyzed in the present paper were retrieved from the HSA[3]. They were collected as part of the CHESS key program, whose observational details are presented extensively in Ceccarelli et al. (2010). Briefly, the Class 0 protostar IRAS 16293-2422 was observed in March 2010 with the HIFI spectrometer (de Graauw et al. 2010; Roelfsema et al. 2012) for a total of 50 h. The targeted coordinates were $\alpha_{2000} = 16^{\rm h}23^{\rm m}22.75^{\rm s}$, $\delta_{2000} = -24°28'34.2''$. Seven different HIFI bands were employed to perform a spectral survey covering the frequency range between 480 and 1902 GHz almost continuously. The observations were carried out in Double-Sideband (DSB) using the wide band spectrometer (WBS), whose resolution is ∼1.1 MHz.

For the present study, we employed bands 1a (488–552 GHz), 2b (724–792 GHz), and 4a (967–1 042 GHz), corresponding to the ID numbers 1342191499, 1342192332, and 1342191619, respectively. The HSA provides level 2.5 data products obtained with the HIFI pipeline of the *Herschel* interactive processing environment (HIPE, Ott 2010). These data generally offer a sufficient scientific quality to perform the line analysis. However, given the weakness of the NHD and ND_2 spectral signals, we also went through the final processing manually. Starting from level 2 products, we inspected all the data, manually removed bad scans, and exported all the "good" 1 GHz chunks into CLASS-GILDAS[4] format. Side-band deconvolution was performed with the minimization algorithm of Comito & Schilke (2002) implemented into CLASS90, and the resulting spectra were cross-checked with the original level 2.5 products. In a few instances, the deconvolution procedure produced a small increase in the noise level compared to the averaged level 2 scans. In such cases, we used the DSB spectra directly after verifying that no interfering emission was present in the image band. At a later stage, intensive baseline subtraction on H- and V-polarisation spectra was applied in the vicinity of each target feature; then, the two sets of data were re-sampled and averaged to obtain the final spectrum.

[1] Heterodyne Instrument for the Far-Infrared.
[2] Chemical *Herschel* surveys of star forming regions.
[3] ESA *Herschel* Science Archive http://archives.esac.esa.int/hsa/whsa.

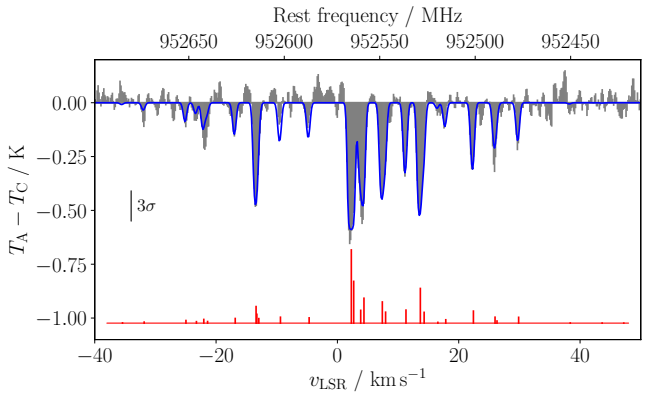

Fig. 1. Spectrum of the $J = \frac{3}{2} - \frac{1}{2}$ component of the $N_{Ka,Kc} = 1_{1,1} - 0_{0,0}$ o-NH_2 transition around 952 GHz observed toward IRAS 16293-2422. The filled gray histograms show the observed spectra, while the blue trace is our HFS fit. The red bars represent the positions of the HFS components assuming LTE intensities.

3. Analysis

The presence of amidogen radical in IRAS 16293-2422 was already established by Hily-Blant et al. (2010) during the early phase of the CHESS key program. We used the results obtained in that study for the parent species NH_2 to test the validity of our data processing and the subsequent spectral analysis. Figure 1 shows the strongest $J = \frac{3}{2} - \frac{1}{2}$ component of the fundamental $N_{Ka,Kc} = 1_{1,1} - 0_{0,0}$ transition of o-NH_2 around 952 GHz. Here, most of the hyperfine structure (HFS) components are resolved and the intensity of the absorption lines is well above the 3σ noise level threshold.

The resulting model of the full HFS (plotted with the solid blue line in Fig. 1) was computed using a custom `Python3` code, which exploits a similar approach to that of the `HFS` method implemented in CLASS. In contrast to the CLASS method, our code uses the column density (N) and the excitation temperature ($T_{\rm ex}$) as fit parameters, and the total opacity of the transition (τ) is regarded as a derived quantity. To this aim, the routine makes use of the physical line parameters and implements the computation of the rotational partition function for any given $T_{\rm ex}$. The set of the fit parameters also includes the line systemic velocity (v_0) in the local standard of rest and the full-width half maximum (FWHM) of the lines (Δv). Briefly, the total line opacity for a given input is first calculated through:

$$\tau = \sqrt{\frac{\ln 2}{16\pi^3}} \frac{c^3 A_{ul} g_u N}{\nu^3 Q_{\rm rot}(T_{\rm ex}) \Delta v} \exp\left(\frac{-E_{\rm low}}{k_{\rm B} T_{\rm ex}}\right) \left[1 - \exp\left(\frac{-h\nu_0}{k_{\rm B} T_{\rm ex}}\right)\right], \quad (1)$$

[4] See GILDAS home page at the URL: http://www.iram.fr/IRAMFR/GILDAS.

Table 1. Summary of the transitions observed for NH_2, NHD, and ND_2 toward IRAS 16293-2422.

Species	Transition $N_{K_a,Kc}, J$	Frequency [a] [GHz]	HPBW [b] [arcsec]	T_C [K]	T_{ex} [K]	v_{LSR} [km s^{-1}]	Δv [c] [km s^{-1}]	N [10^{13} cm^{-2}]	τ [d]
o-NH_2	$1_{1,1}, \frac{3}{2} - 0_{0,0}, \frac{1}{2}$	952.5722	22.4	0.81	8.6(1)	4.096(9)	0.67(8)	5.3(3)	20.3(13)
	$1_{1,1}, \frac{1}{2} - 0_{0,0}, \frac{1}{2}$	959.5043	22.1	0.82	8.8(3)	4.077(9)	0.66(8)	6.8(9)	13.0(12)
NHD	$1_{1,1}, \frac{3}{2} - 0_{0,0}, \frac{1}{2}$	770.7422	27.5	0.55	7.4(1)	4.19(3)	0.78(11)	4.4(6)	10.3(15)
	$1_{1,1}, \frac{1}{2} - 0_{0,0}, \frac{1}{2}$	776.0177	27.3	0.56	7.4	4.10(3)	0.78	5.0(3)	5.8(5)
p-ND_2	$2_{1,2}, \frac{5}{2} - 1_{0,1}, \frac{3}{2}$	784.9317	27.0	0.57	7.4	4.23(4)	0.78	0.23(1)	2.4(2)
	$2_{1,2}, \frac{3}{2} - 1_{0,1}, \frac{1}{2}$	786.8526	26.9	0.57	7.4	4.31(6)	0.78	0.27(2)	1.5(2)
o-ND_2	$1_{1,1}, \frac{3}{2} - 0_{0,0}, \frac{1}{2}$	527.1808	40.2	0.20	4.5	3.98(7)	0.83	0.66(8)	2.0(3)

Notes. Numbers in parentheses refer to 1σ uncertainties expressed in units of the last quoted digit. [a]Rest frequency corresponding to the hypothetically unsplit fine-structure transition. [b]Half-power beam width of the observations. [c]A conservative uncertainty of 0.25 MHz produced by the HIPE pipeline is summed in quadrature. [d]Derived through Eq. (1).

where ν_0 is the rest frequency of the (unsplit) rotational transition, c is the speed of light, $Q_{rot}(T_{ex})$ is the rotational partition function at T_{ex}, g_u is the degeneracy of the upper level, A_{ul} is the Einstein coefficient for spontaneous emission, E_{low} is the energy of the lower state, h is the Planck constant, and k_B is the Boltzmann constant. Then, assuming the local thermodynamic equilibrium (LTE) approximation and Gaussian profiles, the opacity of the ith HFS components is computed as $\tau_i = \tau R_i$, where R_i is the corresponding normalized relative intensity. The ith component opacity at each velocity channel is then given by:

$$\tau_i(v) = \tau_i \exp\left[-4 \ln 2 \left(\frac{v - v_{0,i}}{\Delta v}\right)^2\right], \quad (2)$$

where $v_{0,i}$ is the corresponding velocity position expressed as an offset with respect to the systemic velocity v_0. Finally, the continuum-subtracted antenna temperature at a given velocity channel v is modeled as

$$T_{ant}(v) = [J_\nu(T_{ex}) - J_\nu(T_{CMB}) - T_C]\left(1 - e^{-\sum_i \tau_i(v)}\right), \quad (3)$$

where $J_\nu(T)$ is the Rayleigh–Jeans radiation temperature, T_C is the temperature of the continuum, and T_{CMB} is the cosmic background temperature. These data were compared to the continuum-subtracted observed antenna temperatures, $T_A - T_C$, in a non-linear least-squares fashion to determine the best fit values of N, T_{ex}, Δv, and v_0. Whenever possible, all four parameters were adjusted during the analysis. This sometimes produced a strong correlation between them, especially when fitting weak features (e.g., those of ND_2), for which the relative intensities of the observed HFS components are poorly constrained because of the low signal-to-noise ratio (S/N). In these cases, suitable assumptions for T_{ex} and Δv had to be used and the corresponding parameters were kept fixed in the least-squares fit. The single-sideband continuum temperature T_C, inserted in the radiative transfer equality of Eq. (3), was estimated using the linear formula given by Hily-Blant et al. (2010), $T_C/[\mathrm{K}] = 1.10\,\nu - 0.42$, with ν expressed in THz.

The spectroscopic data for NH_2, NHD, and ND_2 were taken from the most recent laboratory studies (Martin-Drumel et al. 2014; Bizzocchi et al. 2020; Melosso et al. 2017), and the Q_{rot} values used in Eq. (1) were computed at any given temperature by cubic interpolation on a grid of finely spaced entries spanning the 2.7–19 K interval. These were obtained by direct summation on all rotational levels through the SPCAT spectral tool (Pickett 1991), with the ortho and para species of the symmetric isotopologues NH_2 and ND_2 treated separately. A brief explanation of the energy level structures of NHD and ND_2 is given in Appendix A, while the complete list of HFS components used for the analysis of each transition is reported in Appendix C. The partition function values of both species computed at temperatures between 2.725 and 300 K are given in Appendix B.

4. Results

The line parameters obtained from the analysis of the observed transitions of NH_2, NHD, and ND_2 are collected in Table 1. In the first two rows, the results obtained for the fine-structure line of o-NH_2 previously detected by Hily-Blant et al. (2010) are reported. Our fitted N and T_{ex} values compare very well with those obtained from the CLASS HFS method employed in that study. Our weighted average of the column density is $(5.4 \pm 0.4) \times 10^{13}$ cm^{-2}, which is consistent with the value of $(4.4 \pm 0.7) \times 10^{13}$ cm^{-2} obtained previously. The excitation temperatures determined for the two components are 1σ coincident (8.44 ± 0.12 K on average) and are also close to the ones obtained by Hily-Blant et al. (2010) (8.5 K for the $J = \frac{3}{2} - \frac{1}{2}$ and 9.5 K for $J = \frac{1}{2} - \frac{1}{2}$).

In the same spectral survey, we detect, for the first time, two groups of hyperfine transitions belonging to the singly deuterated form of the amidogen radical, NHD. Figure 2 shows the two fine-structure components of the fundamental $N_{Ka,Kc} = 1_{1,1} \leftarrow 0_{0,0}$ transition of NHD, both observed in absorption around 770 and 776 GHz in the 2b HIFI band.

Since the $J = \frac{3}{2} - \frac{1}{2}$ fine-structure line is detected at the ca. 10σ level, we could adjust all four parameters in the model. The $J = \frac{1}{2} - \frac{1}{2}$ component is about twice as weak and its detection is only at the ca. 5σ level. In this case, the noise prevented us from adjusting T_{ex} and Δv, which were then fixed at the values obtained for the strongest component of the fine-structure doublet. For NHD, we find an excitation temperature of 7.4 ± 0.1 K, slightly lower than that of NH_2. This small difference was likely produced by the bigger *Herschel* beam size in the 2b band (~27″) compared to that in the 4a band (~22″). Indeed, a larger region is sampled for the NHD lines, and the contribution of the

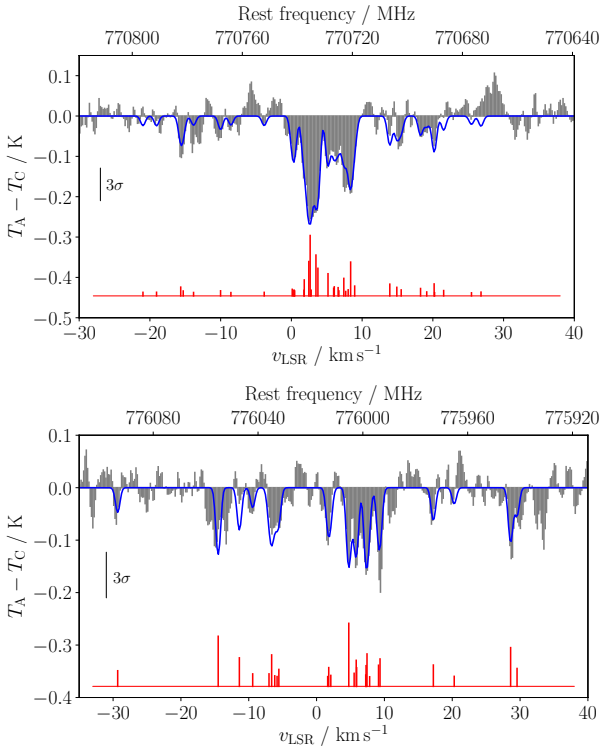

Fig. 2. Spectra of the fine components of the $N_{Ka,Kc} = 1_{1,1} \leftarrow 0_{0,0}$ NHD transition observed toward IRAS 16293-2422. *Upper panel*: $J = \frac{3}{2} - \frac{1}{2}$ component at ca. 770 GHz. *Lower panel*: $J = \frac{1}{2} - \frac{1}{2}$ component at ca. 776 GHz. The filled gray histograms show the observed spectra, while the blue trace is our HFS fit. The red bars represent the positions of the HFS components assuming LTE intensities.

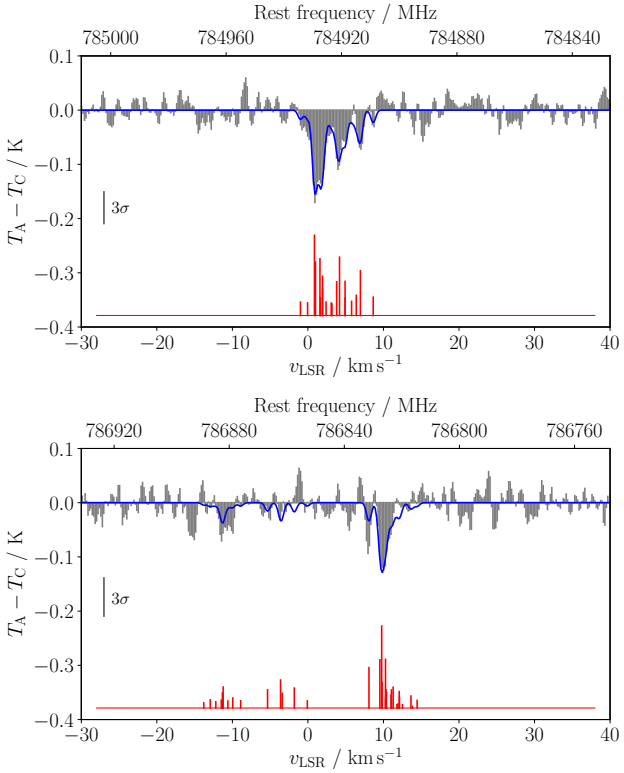

Fig. 3. Spectra of the fine-structure components of the $N_{Ka,Kc} = 2_{1,2} \leftarrow 1_{0,1}$ p-ND_2 transition observed toward IRAS 16293-2422. *Upper panel*: $J = \frac{5}{2} - \frac{3}{2}$ component at ca. 785 GHz. *Lower panel*: $J = \frac{3}{2} - \frac{1}{2}$ component at ca. 787 GHz. The filled gray histograms show the observed spectra, while the blue trace is our HFS fit. The red bars represent the positions of the HFS components assuming LTE intensities.

inner warmer gas is expected to be slightly smaller. The average value of the column density is $N = (4.7 \pm 0.7) \times 10^{13}$ cm^{-2}.

Compared to the parent isotopologue, the doubly deuterated form of amidogen has a denser spectrum in the submillimeter region, thus both the $N_{Ka,Kc} = 1_{1,1} \leftarrow 0_{0,0}$ and $N_{Ka,Kc} = 2_{1,2} \leftarrow 1_{0,1}$ rotational lines fall within the coverage of the CHESS spectral survey. A clear detection was obtained in the 2b band for both the $J = \frac{5}{2} - \frac{3}{2}$ and $J = \frac{3}{2} - \frac{1}{2}$ fine-structure components of the $N_{Ka,Kc} = 2_{1,2} \leftarrow 1_{0,1}$ transitions of the para species. They are shown in Fig. 3. The $N_{Ka,Kc} = 1_{1,1} \leftarrow 0_{0,0}$, $J = \frac{3}{2} - \frac{1}{2}$ of the ortho species, illustrated in Fig. 4, is located at 527 GHz.

In this spectral region, covered by the HIFI 1a band, the continuum emission of the source is only 200 mK; hence, the resulting absorption feature is rather faint and the detection is only marginal, reaching at most 5σ. The other fine-structure component (intrinsically less intense) is just below the noise level and is not detected. Given the weakness of all three components observed for ND_2, their analysis had to be carried out by adopting suitable assumptions for T_{ex} and Δv, as these parameters could not be set as free in the least-squares fits. Given the similarity of the beam size (~27″) for the p-ND_2 $N_{Ka,Kc} = 2_{1,2} \leftarrow 1_{0,1}$ lines, we assumed the same excitation temperature as determined for NHD. A smaller value was expected to hold for the o-ND_2 $N_{Ka,Kc} = 1_{1,1} \leftarrow 0_{0,0}$ line, as the *Herschel*'s half-power beam width (HPBW) at this frequency is as broad as 40″, thus sampling a comparatively large volume of cold gas. For this transition we fixed $T_{ex} = 4.5$ K, a value determined for ND in the same source (Bacmann et al. 2010), through the analysis of its $N = 1-0$ fine-structure doublet centered at 534 GHz. In fact, this value allows for a satisfactory fit of the absorption o-ND_2

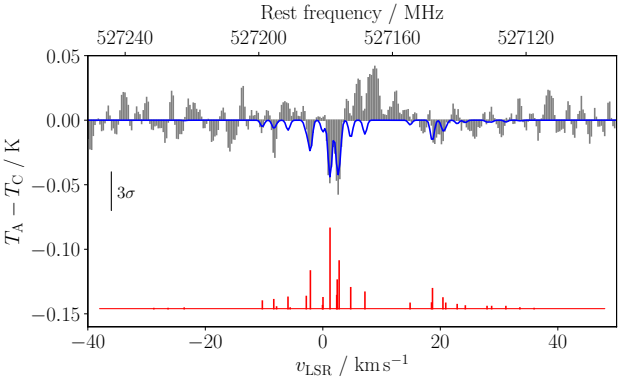

Fig. 4. Spectrum of the $J = \frac{3}{2} - \frac{1}{2}$ component of the $N_{Ka,Kc} = 1_{1,1} - 0_{0,0}$ o-ND_2 transition around 527 GHz observed toward IRAS 16293-2422. The filled gray histograms show the observed spectra, while the blue trace is our HFS fit. The red bars represent the positions of the HFS components assuming LTE intensities.

feature, whereas for higher excitation temperatures (e.g., already at 5.5 K) the LTE model predicts the line to be observable in emission. Constraints for the FWHM line width Δv were derived from the values determined for NH_2 after deconvolution from the WBS resolution (1.1 MHz). The column densities derived for p-ND_2 using two components are consistent within 2σ, and the weighted average value is $N = (0.241 \pm 0.014) \times 10^{13}$ cm^{-2}. The observed ortho-to-para ratio is 2.7 ± 0.4. By considering (i) as the energy difference of 10.77 cm^{-1} ($E/k \approx 15.5$ K) between the lowest para and ortho rotational levels, and (ii) as the spin

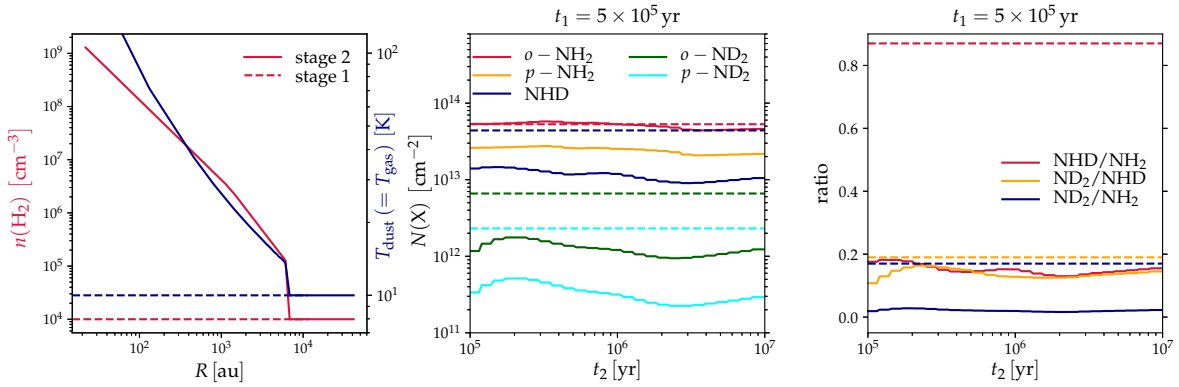

Fig. 5. *Left panel*: density (red) and temperature (blue) structure in the IRAS16293 source model in stages 1 and 2 (see Sect. 5 for details). *Middle panel*: modeled beam-convolved molecular column densities (solid lines, labeled in the plot) as functions of time in stage 2. Dashed lines represent the observed values, omitting error bars for clarity. *Right panel*: modeled D/H ratios (solid lines, labeled in the plot) as functions of time in stage 2. Here, the NH_2 and ND_2 abundances have been summed over the ortho and para forms. Dashed lines represent the observed values, for which the error bars have again been omitted.

statistical weights, this ratio corresponds to an equilibrium temperature of 9 ± 1 K. Due to the different beam sizes used to observe the $N_{Ka,Kc} = 1_{1,1} \leftarrow 0_{0,0}$, and $2_{1,2} \leftarrow 1_{0,1}$ transitions, the p-ND_2 is preferentially sampled in the inner warmer region; therefore, this value is likely to be slightly overestimated.

For the same reason, the evaluation of the abundance ratios between amidogen isotopologues requires some careful considerations. From the averaged N values, we obtained $[NHD]/[NH_2] = 0.87 \pm 0.14$, hinting at a very high deuteration level for amidogen lying in the 70–100% range. We consider this result to be robust. The HPBW of the observations differs by only 25%, thus the source area sampled by the antenna is similar for both the NHD and NH_2 lines. Furthermore, the energy difference between ortho and para species of NH_2 is 21.11 cm^{-1} ($E/k_B \approx 30.4$ K), and the contribution of the unobserved p-NH_2 is expected to be less than 5% at 10 K. Finally, since the used transitions have their lower level located at "zero" energy, the product of two exponential terms in Eq. (1) tends to 1 for small $h\nu_0/k_B T_{ex}$, and the relation between N and τ depends only moderately on the temperature. Hence, the retrieved column density values are not much affected by the inaccuracies in the corresponding T_{ex} determination.

The derivation of sound values of the isotopic ratios involving ND_2 is less straightforward, as various approaches can be adopted to estimate the overall ND_2 column density from the available observational results. By assuming that the two spin species are in thermal equilibrium, total N values of 0.70×10^{13} and 0.98×10^{13} cm^{-2} can be obtained from the o-ND_2 and p-ND_2 results, respectively. A direct sum of the ortho and para column densities with no assumptions gives instead 0.90×10^{13} cm^{-2}. Based on the resulting 30% discrepancies, we conservatively quote $N = (0.9 \pm 0.3) \times 10^{13}$ cm^{-2} as the total column density of ND_2. This yields $[ND_2]/[NHD] = 0.19 \pm 0.07$ and $[ND_2]/[NH_2] = 0.17 \pm 0.06$, that is, deuteration levels in the 10–30% range. The amidogen D/H ratio measured in the low-mass protostar IRAS16293 is very high and is comparable to the one derived for the related species imidogen ($[ND]/[NH] = 30–70\%$, Bacmann et al. 2010), while ammonia shows a lower level ($[NH_2D]/[NH_3] \sim 10\%$, van Dishoeck et al. 1995). The ND_2 species is very abundant, yielding a remarkably high deuteration ratio, even higher than the one found for methanol ($[CHD_2OH]/[CH_3OH] = 6\%$, Parise et al. 2004), a species for which the triply deuterated species was also detected in this source.

5. Chemical simulation

A steady-state model of cold and CO-depleted clouds was published by Roueff et al. (2005), but their predictions on deuterium enhancement (i.e., 10% for NHD and less than 1% for ND_2) are significantly underestimated with respect to our findings, which are 87 and 18% for NHD and ND_2, respectively.

In an effort to reproduce the observed tendencies of the D/H and spin-state abundance ratios, we carried out new chemical simulations of (deuterated) amidogen using a model of IRAS 16293-2422. We followed the approach described in Brünken et al. (2014) and Harju et al. (2017), where more details can be found; we provide only a brief description of the simulations here. For the source model, we adopted the one used in the above references, where the physical model from Crimier et al. (2010), which represents the protostellar core, was extended with a layer of gas representing the molecular cloud that the protostellar system lies within (with $n(H_2) = 10^4$ cm^{-3} and $T_{dust} = T_{gas} = 10$ K). The source model is illustrated in Fig. 5. We considered a two-stage model, in which the chemical evolution was first calculated over time t_1 in physical conditions corresponding to the core extension (stage 1); then the protostellar core model, including the low-density extension, was run over time t_2 (stage 2) using the initial chemical abundances obtained from stage 1. We explored a range of t_1 and t_2 values to search for the best fit to the observed column densities.

The simulation results depend on how the chemical reactions related to (deuterated) amidogen formation are assumed to proceed. Here we used our gas-grain chemical code (Sipilä et al. 2019a) and ran a parameter-space exploration, testing the effects of multi-layer (three-phase) ice chemistry (Sipilä et al. 2016) and a direct proton-deuteron hop (Sipilä et al. 2019b), as opposed to full scrambling in proton-donation reactions (Sipilä et al. 2015), on the various column densities. As an example of the results, Fig. 5 shows a comparison of the beam-convolved modeled and observed column densities with column density ratios using the multi-layer ice model and full scrambling for proton-donation reactions. The chemical model reproduces the column density of o-NH_2 and the ND_2/NHD ratio very well, but fails to reproduce the NHD/NH_2 ratio or the NHD and (ortho and para) ND_2 column densities. Other parameter combinations instead reproduce the NHD and (ortho and para) ND_2 column densities very well, but strongly overpredict the o-NH_2 column density. None of the parameter combinations we explored led to

the observed level for the NHD/NH_2 ratio. The chemical model predicts that most of the NHD column originates near the edge of the protostellar core, where the temperature in the source model (∼14 K at the very edge, rising inward; cf. Fig. 5) inhibits NHD production with respect to NH_2. Indeed, an NHD/NH_2 ratio of unity or above can be produced by the chemical model if the gas is sufficiently dense ($n(H_2) \gtrsim 10^5$ cm^{-3}) and cold ($T \sim 10$ K), suggesting that our two-phase approach to the core modeling is inadequate for the modeling of amidogen chemistry, and that a substantial amount of time (on the order of 10^6 yr) is required in the pre-stellar phase for the NHD/NH_2 ratio to increase to the observed level. We stress that in the present work we did not carry out radiative transfer simulations of the amidogen absorption lines, and therefore the comparison of the modeled column densities against the observed ones does not take into account any excitation effects. We will present an in-depth comparison of the model versus the observations in an upcoming work, where we will also carry out line simulations.

6. Discussion and conclusions

This work presents the very first detection of both deuterated forms of amidogen radical in the ISM. Column densities and deuterium fractionation values were derived from the observations, allowing for a direct comparison with the predictions obtained from chemical networks. We ran a parameter-space exploration using our gas-grain chemical code, implementing a two-stage approach to the dynamical evolution of the source. The observed abundances of all NH_2, NHD, and ND_2 isotopic variants could not be simultaneously reproduced with a single set of modeling parameters, indicating that the two-stage approach to the core modeling is inadequate for simulating amidogen isotopic chemistry. More insights on this topic would come from additional observations of deuterated amidogen isotopologues. The observations are, however, partially hampered by the atmospheric opacity. In fact, the most intense transition of NHD, located at 770 GHz, is not accessible with the ground-based facilities because of strong water absorption lines nearby. Hence, NHD observations can rely mainly on the *a*-type $N_{Ka,Kc} = 1_{0,1} \leftarrow 0_{0,0}$ transition around 413 GHz. Luckily, spectral coverage at this frequency is supported by the ALMA 8 Band and the new nFLASH receiver of APEX. As for ND_2, the transitions detected in this work fall in spectral windows accessible either with the incoming band 1 of the 4GREAT receiver on board SOFIA (490–635 GHz) or the ALMA 10 Band (787–950 GHz).

The conclusions of the present work can be summarized as follows:

1. Thanks to the recently obtained laboratory data, two deuterated forms of amidogen radical, namely NHD and ND_2, were identified for the first time in the ISM. The analysis of hyperfine resolved transitions, observed in absorption against the continuum of the Class 0 protostar IRAS 16293-2422, allowed for the accurate determination of column densities and excitation temperatures.
2. The deuterium fractionation of amidogen results to be 70–100% for NHD and 10–30% for ND_2. Our derived values differ significantly, being larger by about one order of magnitude, from those predicted by earlier astrochemical models.
3. The low temperature and the high degree of deuteration observed suggest that amidogen, similar to other nitrogen-containing species, is less depleted and subsists longer in the gas-phase, thus leading to high abundances of NHD and ND_2.
4. The amidogen D/H and spin-state abundance ratios in IRAS 16293-2422 cannot be reproduced with our gas-grain chemical model unless the pre-stellar stage has a long duration, on the order of one million years.
5. The best candidate to perform future observations of NHD and ND_2, not only in IRAS 16293-2422 but also in other sources where deuterated ammonia has been detected, is ALMA. More observations would enable us to take a step toward a thorough understanding of ammonia formation and deuteration in the ISM.

Acknowledgements. This study was supported by Bologna University (RFO funds) and by MIUR (Project PRIN 2015: STARS in the CAOS, Grant Number 2015F59J3R). The work at SOLEIL was supported by the Programme National "Physique et Chimie du Milieu Interstellaire" (PCMI) of CNRS/INSU with INC/INP co-funded by CEA and CNES.

References

Bacmann, A., Caux, E., Hily-Blant, P., et al. 2010, A&A, 521, L42
Bacmann, A., Daniel, F., Caselli, P., et al. 2016, A&A, 587, A26
Bizzocchi, L., Melosso, M., Giuliano, B. M., et al. 2020, ApJS, 247, 59
Brown, J., Chalkley, S., & Wayne, F. 1979, Mol. Phys., 38, 1521
Brünken, S., Sipilä, O., Chambers, E. T., et al. 2014, Nature, 516, 219
Butner, H., Charnley, S., Ceccarelli, C., et al. 2007, ApJ, 659, L137
Caselli, P., & Ceccarelli, C. 2012, A&ARv, 20, 56
Ceccarelli, C., Castets, A., Loinard, L., Caux, E., & Tielens, A. 1998, A&A, 338, L43
Ceccarelli, C., Caselli, P., Herbst, E., Tielens, A. G. G. M., & Caux, E. 2007, in Protostars and Planets V, eds. B. Reipurth, D. Jewitt, & K. Keil (Tucson, AZ: University of Arizona Press), 47
Ceccarelli, C., Bacmann, A., Boogert, A., et al. 2010, A&A, 521, L22
Ceccarelli, C., Caselli, P., Bockelée-Morvan, D., et al. 2014, Protostars and Planets VI (Tucson, AZ: University of Arizona Press), 859
Comito, C., & Schilke, P. 2002, A&A, 395, 357
Crimier, N., Ceccarelli, C., Maret, S., et al. 2010, A&A, 519, A65
de Graauw, T., Helmich, F. P., Phillips, T. G., et al. 2010, A&A, 518, L6
Fayolle, E. C., Öberg, K. I., Jørgensen, J. K., et al. 2017, Nat. Astron., 1, 703
Harju, J., Sipilä, O., Brünken, S., et al. 2017, ApJ, 840, 63
Hily-Blant, P., Maret, S., Bacmann, A., et al. 2010, A&A, 521, L52
Jørgensen, J. K., Favre, C., Bisschop, S. E., et al. 2012, ApJ, 757, L4
Kanada, M., Yamamoto, S., & Saito, S. 1991, J. Chem. Phys., 94, 3423
Kobayashi, K., Ozeki, H., Saito, S., Tonooka, M., & Yamamoto, S. 1997, J. Chem. Phys., 107, 9289
Linsky, J. L. 2003, in Solar System History from Isotopic Signatures of Volatile Elements (Berlin: Springer), 49
Loinard, L., Castets, A., Ceccarelli, C., Caux, E., & Tielens, A. 2001, ApJ, 552, L163
Martin-Drumel, M. A., Pirali, O., & Vervloet, M. 2014, J. Phys. Chem. A, 118, 1331
Melosso, M., Degli Esposti, C., & Dore, L. 2017, ApJS, 233, 1
Melosso, M., Bizzocchi, L., Tamassia, F., et al. 2019a, Phys. Chem. Chem. Phys., 21, 3564
Melosso, M., Conversazioni, B., Degli Esposti, C., et al. 2019b, J. Quant. Spectr. Rad. Transf., 222, 186
Melosso, M., Dore, L., Gauss, J., & Puzzarini, C. 2020, J. Mol. Spectr., 370, 111291
Ott, S. 2010, ASP Conf. Ser., 434, 139
Parise, B., Castets, A., Herbst, E., et al. 2004, A&A, 416, 159
Pickett, H. M. 1991, J. Mol. Spectr., 148, 371
Roelfsema, P. R., Helmich, F. P., Teyssier, D., et al. 2012, A&A, 537, A17
Roueff, E., Lis, D. C., Van der Tak, F., Gerin, M., & Goldsmith, P. 2005, A&A, 438, 585
Sipilä, O., Harju, J., Caselli, P., & Schlemmer, S. 2015, A&A, 581, A122
Sipilä, O., Caselli, P., & Taquet, V. 2016, A&A, 591, A9
Sipilä, O., Caselli, P., Redaelli, E., Juvela, M., & Bizzocchi, L. 2019a, MNRAS, 487, 1269
Sipilä, O., Caselli, P., & Harju, J. 2019b, A&A, 631, A63
van der Tak, F. F. S., Schilke, P., Müller, H. S. P., et al. 2002, A&A, 388, L53
van Dishoeck, E. F., Blake, G. A., Jansen, D. J., et al. 1995, ApJ, 447, 760
Vastel, C., Phillips, T., Ceccarelli, C., & Pearson, J. 2003, ApJ, 593, L97

Appendix A: Energy level scheme

A.1. Singly deuterated amidogen radical

The manifold of rotational energy levels is very complex in NHD and its spectrum is characterized by many interactions. First, NHD is a light asymmetric rotor far from the prolate limit ($\kappa = -0.66$), whose electric dipole moment lies in the *ab* principal symmetry plane, with components $\mu_a = 0.67$ D and $\mu_b = 1.69$ D (Brown et al. 1979). Because of the large values of the rotational constants, the room temperature spectrum is quite sparse and peaks in the far-infrared (FIR) region.

Furthermore, NHD is an open-shell molecule with an $\tilde{X}\,^2A''$ ground electronic state. Due to the presence of an unpaired electron, the electronic spin ($\mathbf{S} = 1/2$) couples with the rotational angular momentum $\mathbf{N}$, thus splitting each rotational level N_{K_a,K_c} into two fine-structure sub-levels. The fine-structure levels have either $J = N + 1/2$ or $J = N - 1/2$ quantum numbers, with the exception of the $N = 0$ level, for which only the $J = 1/2$ level exists. The total angular momentum $\mathbf{J}$ further couples with each nuclear spin (I_N and $I_D = 1$, $I_H = 1/2$), giving rise to the so-called hyperfine structure (HFS). The adopted angular momentum coupling scheme takes into account the magnitude of the interaction (from strongest to weakest):

$$\mathbf{J} = \mathbf{N} + \mathbf{S}, \tag{A.1a}$$
$$\mathbf{F}_1 = \mathbf{J} + \mathbf{I}_N, \tag{A.1b}$$
$$\mathbf{F}_2 = \mathbf{F}_1 + \mathbf{I}_H, \tag{A.1c}$$
$$\mathbf{F} = \mathbf{F}_2 + \mathbf{I}_D. \tag{A.1d}$$

A more detailed account of the NHD spectroscopy can be found in Bizzocchi et al. (2020).

A.2. Doubly deuterated amidogen radical

The higher symmetry of ND_2 with respect to NHD requires additional considerations in the description of the energy level manifold. The species ND_2 belongs to the C_{2v} symmetry point group, and a π-rotation along the *b* axis exchanges the two identical deuterium nuclei. Since deuterium is a boson, the total wave-function of ND_2 must be symmetric upon the permutation of the two particles. Given that the electronic ground state is antisymmetric ($\tilde{X}\,^2B_1$) and the vibrational ground state is symmetric, deuterium nuclear spin functions ($I_{D,tot} = I_{D_1} + I_{D_2}$) can only combine with rotational levels of opposite symmetry. That is, symmetric rotational levels ($K_a + K_c$ = even) combine with antisymmetric deuterium spin functions with $I_{D,tot} = 1$ (ortho states), while antisymmetric rotational levels ($K_a + K_c$ = odd) combine with the spin functions $I_{D,tot} = 0,\ 2$ (para states). Only transitions within the states are allowed by the permanent electric dipole moment of ND_2 ($\mu_b = 1.82(5)$ D Brown et al. 1979). At low temperatures, given the energy difference of 15.5 K between the ortho and para states, o-ND_2 and p-ND_2 should be considered as different species.

The network of fine and hyperfine interactions in ND_2 is analogous to that described earlier for NHD, while the coupling scheme of angular momentum changes as follows:

$$\mathbf{F}_1 = \mathbf{J} + \mathbf{I}_N, \tag{A.2a}$$
$$\mathbf{F} = \mathbf{F}_1 + \mathbf{I}_{D,tot}. \tag{A.2b}$$

A detailed account of the spectroscopic features of ND_2 can be found in Melosso et al. (2017).

Appendix B: Partition function values

Table B.1. Rotational partition function values of NHD and ND_2 computed at different temperatures.

Temperature (K)	NHD	ND_2
300.000	6420.8713	7580.4217
225.000	4176.0818	4927.1928
150.000	2283.1782	2689.7500
75.000	820.8872	962.6221
37.500	301.1282	349.7845
18.750	115.5024	130.1662
9.375	52.9533	48.8603
5.000	38.1321	23.5653
2.725	36.0453	18.3627

The spectroscopic parameters from Bizzocchi et al. (2020) and Melosso et al. (2017) were input into the SPCAT subroutine (Pickett 1991) to evaluate the rotational partition function of NHD and ND_2, respectively. All energy levels up to $J = 20$ and $K_a = 15$ were considered. The temperature-dependence of Q_{rot} was computed analytically for both species at temperatures between 2.725 and 300 K. These values are given in Table B.1.

Appendix C: List of the used HFS components

Tables C.1–C.5 list the rest frequencies of the observed hyperfine components of NHD and ND_2. The LTE intensities (computed at 300 K and labeled LGINT in the tables) and the HFS quantum numbers are also given. Spectral predictions are based on the spectroscopic studies reported in Melosso et al. (2017) and in Bizzocchi et al. (2020).

Table C.1. HFS components used to reproduce the $J = \frac{3}{2} \leftarrow \frac{1}{2}$, $N_{Ka,Kc} = 1_{1,1} \leftarrow 0_{0,0}$ transition of NHD.

Frequency	LGINT	Up. state			Lo. state		
(MHz)	(nm^2 MHz)	F'_1	F'_2	F'	F_1	F_2	F
770 684.033	−3.5757	0.5	0	1	1.5	1	1
770 697.605	−3.4229	1.5	1	2	1.5	1	1
770 701.070	−3.0725	1.5	1	2	1.5	1	2
770 703.764	−3.5532	1.5	1	0	1.5	1	1
770 706.007	−3.2813	1.5	1	1	1.5	1	2
770 713.045	−3.3739	1.5	2	1	1.5	2	1
770 714.635	−3.2184	1.5	2	2	1.5	2	2
770 717.184	−3.0809	1.5	2	3	1.5	2	3
770 729.939	−3.1592	0.5	1	2	0.5	1	2
770 731.407	−2.6209	2.5	2	3	1.5	1	2
770 732.303	−3.3683	0.5	1	1	0.5	1	1
770 733.192	−3.5106	0.5	1	1	0.5	1	0
770 733.891	−2.9068	2.5	2	2	1.5	1	1
770 735.685	−3.4570	0.5	1	0	0.5	1	1
770 735.961	−3.2356	2.5	2	1	1.5	1	0
770 737.355	−3.1949	2.5	2	2	1.5	1	2
770 737.593	−3.2680	2.5	2	1	1.5	1	1
770 739.631	−2.8049	0.5	1	2	0.5	0	1
770 743.306	−2.7096	2.5	3	2	1.5	2	1
770 744.024	−2.5392	2.5	3	3	1.5	2	2
770 745.755	−3.3952	0.5	1	1	0.5	0	1
770 746.127	−2.3691	2.5	3	4	1.5	2	3
770 746.604	−2.6141	1.5	2	3	0.5	1	2
770 748.263	−2.9477	1.5	2	2	0.5	1	1
770 748.379	−3.4022	2.5	3	2	1.5	2	2
770 751.746	−3.4616	1.5	2	1	0.5	1	1
770 751.990	−3.3905	2.5	3	3	1.5	2	3
770 752.022	−3.4349	1.5	2	2	0.5	1	2
770 752.634	−3.3344	1.5	2	1	0.5	1	0
770 762.836	−3.6026	1.5	1	2	1.5	2	3
770 778.684	−3.4439	0.5	0	1	0.5	1	2
770 792.256	−3.4614	1.5	1	2	0.5	1	2
770 793.173	−3.2079	2.5	2	3	1.5	2	3
770 801.949	−3.5909	1.5	1	2	0.5	0	1
770 806.886	−3.6006	1.5	1	1	0.5	0	1

Table C.2. HFS components used to reproduce the $J = \frac{1}{2} \leftarrow \frac{1}{2}$, $N_{Ka,Kc} = 1_{1,1} \leftarrow 0_{0,0}$ transition of NHD.

Frequency	LGINT	Up. state			Lo. state		
(MHz)	(nm^2 MHz)	F'_1	F'_2	F'	F_1	F_2	F
775 951.7799	−3.3743	1.5	2	2	1.5	1	1
775 954.2373	−3.0381	1.5	2	3	1.5	1	2
775 983.7269	−3.2975	1.5	1	2	1.5	2	3
776 004.0628	−3.1888	0.5	1	2	1.5	1	2
776 004.6459	−3.3020	1.5	2	1	1.5	2	1
776 009.0444	−3.1157	1.5	2	2	1.5	2	2
776 009.3879	−3.3118	1.5	1	2	0.5	1	1
776 009.5205	−3.5730	0.5	0	1	1.5	1	1
776 012.9847	−3.3589	0.5	0	1	1.5	1	2
776 013.1471	−3.2111	1.5	1	2	0.5	1	2
776 013.9374	−3.5115	1.5	1	1	0.5	1	2
776 016.0039	−2.8268	1.5	2	3	1.5	2	3
776 022.8395	−3.5879	1.5	1	2	0.5	0	1
776 023.6298	−3.3538	1.5	1	1	0.5	0	1
776 042.6716	−3.3983	1.5	2	2	0.5	1	1
776 044.2348	−3.6053	1.5	2	1	0.5	1	0
776 045.4241	−3.1291	1.5	2	3	0.5	1	2
776 046.4309	−3.5307	1.5	2	2	0.5	1	2
776 052.6624	−3.5309	0.5	1	0	1.5	2	1
776 057.7495	−3.1714	0.5	1	1	1.5	2	2
776 065.8293	−2.9268	0.5	1	2	1.5	2	3
776 104.1715	−3.4331	0.5	0	1	0.5	1	2

Table C.3. HFS components used to reproduce the $J = \frac{3}{2} \leftarrow \frac{1}{2}$, $N_{Ka,Kc} = 1_{1,1} \leftarrow 0_{0,0}$ transition of ND_2.

Frequency	LGINT	Up. state			Lo. state		
(MHz)	(nm^2 MHz)	F'_1	$I'_{D,tot}$	F'	F_1	$I_{D,tot}$	F
527 133.0435	−4.2749	0.5	1	0.5	1.5	1	0.5
527 137.3007	−4.2731	0.5	1	0.5	1.5	1	1.5
527 138.6811	−4.2681	0.5	1	1.5	1.5	1	2.5
527 145.1770	−4.1674	1.5	1	2.5	1.5	1	1.5
527 147.6220	−3.9877	1.5	1	1.5	1.5	1	0.5
527 151.0397	−3.8630	1.5	1	0.5	1.5	1	0.5
527 151.8792	−3.5628	1.5	1	1.5	1.5	1	1.5
527 155.0073	−3.2897	1.5	1	2.5	1.5	1	2.5
527 155.2969	−3.8423	1.5	1	0.5	1.5	1	1.5
527 161.7095	−3.8657	1.5	1	1.5	1.5	1	2.5
527 175.2302	−3.3744	0.5	1	1.5	0.5	1	1.5
527 179.4875	−3.2692	0.5	1	1.5	0.5	1	0.5
527 182.9457	−2.9117	2.5	1	2.5	1.5	1	1.5
527 183.5235	−3.1343	2.5	1	1.5	1.5	1	0.5
527 183.6802	−3.4747	0.5	1	0.5	0.5	1	1.5
527 185.6745	−2.6845	2.5	1	3.5	1.5	1	2.5
527 187.7807	−3.5532	2.5	1	1.5	1.5	1	1.5
527 187.9375	−4.1230	0.5	1	0.5	0.5	1	0.5
527 191.5565	−3.0134	1.5	1	2.5	0.5	1	1.5
527 192.7760	−3.5051	2.5	1	2.5	1.5	1	2.5
527 198.2587	−3.5357	1.5	1	1.5	0.5	1	1.5
527 201.6764	−4.3765	1.5	1	0.5	0.5	1	1.5
527 202.5160	−3.6385	1.5	1	1.5	0.5	1	0.5
527 205.9337	−3.7120	1.5	1	0.5	0.5	1	0.5

Table C.4. HFS components used to reproduce the $J = \frac{5}{2} \leftarrow \frac{3}{2}$, $N_{Ka,Kc} = 2_{1,2} \leftarrow 1_{0,1}$ transition of ND_2.

Frequency	LGINT	Up. state			Lo. state		
(MHz)	(nm^2 MHz)	F'_1	$I'_{D,tot}$	F'	F_1	$I_{D,tot}$	F
784 901.6100	−3.3624	2.5	2	3.5	2.5	2	3.5
784 901.8686	−3.3381	2.5	0	2.5	2.5	0	2.5
784 903.2122	−3.2352	2.5	2	4.5	2.5	2	4.5
784 906.4925	−3.4213	1.5	2	2.5	1.5	2	2.5
784 906.9759	−3.2482	1.5	2	3.5	1.5	2	3.5
784 907.7212	−3.3377	1.5	0	1.5	1.5	0	1.5
784 912.0082	−3.4046	1.5	2	0.5	1.5	2	1.5
784 913.9865	−3.4905	1.5	2	1.5	1.5	2	2.5
784 920.0864	−2.8823	1.5	2	2.5	0.5	2	1.5
784 924.5270	−2.4925	1.5	2	3.5	0.5	2	2.5
784 925.9631	−2.8414	1.5	0	1.5	0.5	0	0.5
784 927.5805	−2.9946	1.5	2	1.5	0.5	2	1.5
784 929.8205	−2.9028	2.5	2	2.5	1.5	2	1.5
784 929.8382	−2.6114	2.5	2	3.5	1.5	2	2.5
784 931.7629	−2.3779	2.5	2	4.5	1.5	2	3.5
784 932.0249	−3.2870	2.5	2	1.5	1.5	2	0.5
784 932.2158	−3.3227	1.5	2	0.5	0.5	2	1.5
784 932.7588	−2.6164	2.5	0	2.5	1.5	0	1.5
784 934.3875	−3.0821	2.5	2	1.5	1.5	2	1.5
784 934.6498	−3.0523	1.5	2	2.5	0.5	2	2.5
784 934.6762	−3.2289	2.5	2	0.5	1.5	2	0.5
784 936.4341	−3.0168	2.5	2	2.5	1.5	2	2.5
784 937.6522	−2.5509	3.5	2	3.5	2.5	2	2.5
784 937.6570	−2.7232	3.5	2	2.5	2.5	2	1.5
784 938.3512	−2.9047	3.5	2	1.5	2.5	2	0.5
784 938.5498	−2.3902	3.5	2	4.5	2.5	2	3.5
784 940.0965	−2.4157	3.5	0	3.5	2.5	0	2.5
784 940.4444	−3.1259	2.5	2	3.5	1.5	2	3.5
784 940.4531	−2.2396	3.5	2	5.5	2.5	2	4.5
784 941.3117	−3.2175	3.5	2	1.5	2.5	2	1.5
784 942.8337	−3.0461	3.5	2	2.5	2.5	2	2.5
784 945.3078	−3.0176	3.5	2	3.5	2.5	2	3.5
784 948.8334	−3.1526	3.5	2	4.5	2.5	2	4.5

Table C.5. HFS components used to reproduce the $J = \frac{3}{2} \leftarrow \frac{1}{2}$, $N_{Ka,Kc} = 2_{1,2} \leftarrow 1_{0,1}$ transition of ND_2.

Frequency	LGINT	Up. state			Lo. state		
(MHz)	(nm^2 MHz)	F'_1	$I'_{D,tot}$	F'	F_1	$I_{D,tot}$	F
786 826.0110	−3.4286	1.5	2	0.5	0.5	2	1.5
786 828.1584	−3.2317	1.5	2	1.5	0.5	2	1.5
786 832.1370	−3.2842	1.5	2	2.5	0.5	2	1.5
786 832.2338	−3.0963	2.5	2	3.5	1.5	2	3.5
786 834.3398	−2.9932	2.5	2	2.5	1.5	2	2.5
786 834.9400	−3.0538	2.5	2	1.5	1.5	2	1.5
786 835.0841	−3.2113	2.5	2	0.5	1.5	2	0.5
786 836.6556	−3.1210	1.5	2	2.5	0.5	2	2.5
786 836.7849	−3.0547	1.5	0	1.5	0.5	0	0.5
786 836.9956	−3.2843	2.5	2	1.5	1.5	2	0.5
786 836.9995	−2.6241	2.5	0	2.5	1.5	0	1.5
786 838.1735	−2.9018	2.5	2	2.5	1.5	2	1.5
786 838.3241	−2.3974	2.5	2	4.5	1.5	2	3.5
786 838.9615	−2.6275	2.5	2	3.5	1.5	2	2.5
786 842.7431	−2.7050	1.5	2	3.5	0.5	2	2.5
786 864.1688	−3.4603	0.5	2	1.5	0.5	2	1.5
786 868.6874	−3.0107	0.5	2	1.5	0.5	2	2.5
786 872.8893	−3.1436	0.5	0	0.5	0.5	0	0.5
786 873.4617	−2.8638	0.5	2	2.5	0.5	2	1.5
786 877.9803	−3.0524	0.5	2	2.5	0.5	2	2.5
786 887.3254	−3.4508	1.5	2	2.5	1.5	2	3.5
786 890.0744	−3.3125	1.5	2	1.5	1.5	2	2.5
786 891.7607	−3.4671	1.5	2	0.5	1.5	2	1.5
786 893.4129	−2.9898	1.5	2	3.5	1.5	2	3.5
786 893.6763	−3.1369	1.5	0	1.5	1.5	0	1.5
786 894.0531	−3.4158	1.5	2	2.5	1.5	2	2.5
786 897.8867	−3.4000	1.5	2	2.5	1.5	2	1.5